RSC Advances

ROYAL SOCIETY OF CHEMISTRY

www.rsc.org/advances

Effect of Acid Functionalised Carbon Supports of Pd-Ni-Sn Catalyst on Ethanol Oxidation Reaction

S. Jongsomjit[a,b], K. Sombatmankhong[c] and P. Prapainainar[b,d,e]

[a]Interdisciplinary Graduate Program in Advanced and Sustainable Environmental Engineering, Kasetsart University, Bangkok 10900, Thailand.

[b]National Center of Excellence for Petroleum, Petrochemicals and Advanced Materials, Department of Chemical Engineering, Faculty of Engineering, Kasetsart University, 50 Ngamwongwan Road, Ladyao, Jatujak, Bangkok 10900, Thailand.

[c]National Metal and Materials Technology Center, 114 Thailand Science Park, Phahonyothin Road, Khlong Nueng, Khlong Luang, Pathum Thani 12120, Thailand.

[d]Center for Advanced Studies in Nanotechnology and Its Applications in Chemical Food and Agricultural Industries, Kasetsart University, 50 Ngamwongwan Road, Ladyao, Jatujak, Bangkok 10900, Thailand.

[e]Department of Chemistry and NANOTEC Center for Nanoscale Materials Design for Green Nanotechnology, Kasetsart University, 50 Ngamwongwan Road, Ladyao, Jatujak, Bangkok 10900, Thailand.

Email; exclusive_boat@hotmail.com, korakots@mtec.co.th, fengpwn@ku.ac.th

Corresponding author; fengpwn@ku.ac.th, tel +6688-020-2494, fax +6682-561-4621

Department of Chemical Engineering, Faculty of Engineering, Kasetsart University, Bangkok 10900, THAILAND.

Abstract

The sodium borohydride reduction method was employed to prepare ternary catalyst with an atomic ratio of 20%Pd10%Ni10%Sn impregnated on four carbon supports including

Vulcan XC-72R carbon black (CB), functionalised carbon black (CB_{sn}), multi-walled carbon nanotubes (MWCNTs) and functionalised MWCNTs ($MWCNT_{sn}$) to improve the catalytic activity for direct ethanol fuel cells (DEFCs). The acid functionalisation was performed using H_2SO_4 and HNO_3. The addition of Ni and Sn metals helped to increase catalytic activity as well as catalyst stability in the ethanol oxidation reaction (EOR). The XRD and XPS results confirmed the presence of $Ni(OH)_2$ and SnO_2 compounds. The crystalline size was in the range of 6.4 to 7.4 nm for all samples. TEM images of catalyst on $MWCNT_{sn}$ confirmed that the catalyst particles were uniformly distributed and dispersed with a particle size in the range of 6 nm. This result was consistent to the highest number of active sites investigated by CO chemisorption. This was due to the high crystalline structure of $MWCNT_{sn}$. Moreover, the catalyst on MWCNTs exhibited the highest current density (291 mA cm^{-2}) for EOR, great catalyst stability, the highest electrochemical surface area (77.155 m^2g^{-1} Pd) and excellent CO tolerance.

Keywords: Pd-Ni-Sn catalyst; electro-oxidation; acid treatment; carbon support; direct ethanol fuel cell.

1 Introduction

Nowadays, the world's demand for energy consumption is dramatically increasing, while the major source of energy coming from fossil fuels is limited and depleting at a faster rate. The use of fossil fuels also raises serious environmental concerns; hence the development of alternative and renewable energy technologies is needed. Among others, fuel cell technology has the potential to contribute to a sustainable and emission-free transport and energy system. A fuel cell produces electricity via electrochemical reaction but without combustion as in conventional combustion processes. A proton exchange membrane fuel cell (PEMFC) is one of the most widely used types of fuel cells being developed for stationary and portable applications, since it offers several benefits, for example, low operating temperature and pressure, low catalyst loading, and high durability [1]. There are various types of fuels being used in PEMFCs, such as hydrogen gas, formic acid, methanol, ethanol, etc. Commercially viable fuel cell systems use hydrogen or direct methanol as a fuel which is depended on their applications. The conventional hydrogen fuel cell is usually used to deliver high power density, whereas the direct methanol fuel cell (DMFC) is more suitable for low power applications [2]. However, ethanol appears to be the preferred candidate fuel over methanol as the energy density and specific energy of ethanol are greatly higher [3, 4]. Moreover, ethanol can be produced at low cost and in large quantities by fermentation of domestic biomass. For these reasons, a direct ethanol fuel cell (DEFC) has become a promising renewable and clean energy device with less influence of catalyst poisoning and fuel crossover when compared to a DMFC [5].

The kinetic rate of ethanol oxidation reaction in alkaline DEFCs is higher than that of DEFCs in acid media[6]. Thus, non-noble metal catalysts such as nickel and silver can be utilized along with low-cost noble metals such as palladium (Pd) and ruthenium (Ru) as anode catalysts[4]. However, electrode poisoning often associated with these anode catalysts is a critical issue in a DEFC. The catalyst instability is caused by the adsorption of CO intermediate generated during ethanol oxidation reaction (EOR). A considerable amount of work has been carried out to find alternative alloys of non-noble and noble metals which yield high EOR activity and durability [7-9]. High selectivity of the anode catalyst is also important as complete oxidation of ethanol to CO_2 is desired to produce the most electrons from one molecule of ethanol[10].

Pd, one of the most abundant noble metals in nature and cheaper than platinum (Pt) by 50%, has been recognized as the most efficient catalyst for EOR in alkaline media[11-14]. Thus, the metal and its alloys serve as substitutes for Pt in catalytic reactions. However, its catalytic stability and activity need to be improved. This can be achieved by introducing binary or ternary catalysts such as Au, Ni, Ru, Sn, Ir, Bi, etc. [15-28]. It has been reported that Ni, Au, or Ru could be used to increase the activity and the stability of Pd while Sn, Ir, or Bi has been used to facilitate the desorption of CO-intermediate during the EOR [29].

The type of catalyst support is also a key factor to enhance the catalytic activity [17, 30]. In general, carbon black is the most widely used catalyst support in DEFCs [12, 31-33]. The average size of the primary particles obtained from pyrolysis or incomplete combustion of carbon compounds is normally in the range of 10-50 nm [34]. The BET surface area (S_{BET}) is in the range of 10-1500 m^2g^{-1}, depending on the method to produce carbon blacks. There are many types of carbon black commercially available, such as acetylene black, Vulcan XC-72, and Ketjenblack. Apart from carbon black supports, varieties of carbon nanotubes are also exploited, including single-walled (SWCNTs) and multi-walled carbon nanotubes (MWCNTs). The unique structure and particular morphologies of nanotubes make them more attractive as catalyst supports for fuel cells. They have high surface area, corrosion resistance, good electro-conductivity, high stability, meso-porosity, and high degree of crytallinity [35-38]. As a result, they have exhibited excellent performance when used as catalyst supports. Treatment with HNO_3 and H_2SO_4 was carried out following Osorio *et al.* procedure [39]. They treated carbon nanotubes in different acids and found that the carbon nanotubes treated by nitric-sulfuric acid and nitric-sulfuric-hydrochloric acid showed good support characteristic.

Based on the preceding, the Pd-based catalysts with Ni and Sn co-catalysts were developed in this present work to increase the catalyst efficiency for DEFC for the first time using sodium borohydride reduction method and also to reduce the cost of catalysts. Moreover, the developed catalysts were prepared on functionalised and non-functionalised carbon based supports. The ternary catalysts with an atomic ratio of 20%Pd10%Ni10%Sn were initially synthesized on different types of carbon supports: (i) Vulcan XC-72R carbon black, (ii) MWCNTs, (iii) functionalised Vulcan XC-72R carbon black, and (iv) functionalised MWCNTs. The catalyst ratio was studied prior to select the most suitable ratio. Physical properties of those carbon supports were examined using temperature program reduction (TPR), chemisorption analysis, Raman spectroscopy, Fourier transform infrared spectroscopy (FT-IR), thermogravimetric analysis (TGA) and scanning electron microscopy–energy dispersion spectroscopy (SEM-EDX). In order to access their suitability for use in DEFC, the 20%Pd10%Ni10%Sn deposited on different supports were investigated using X-ray diffraction (XRD), transmission electron microscopy (TEM), SEM-EDX, X-ray photoelectron spectroscopy (XPS), and CO-pulse and TPR chemisorption analysis. Additionally, several modes of voltammetry were performed to explore their catalytic activity, CO tolerance, durability, and electrochemical surface area.

2 Materials and Methods

2.1 Materials

The metal precursors for anode electro-catalysts were prepared from palladium chloride ($PdCl_2$), nickel chloride ($NiCl_2$), and tin chloride ($SnCl_2$), which were purchased from Merck. Sodium borohydride ($NaBH_4$) was purchased from HiMedia. Carbon black (Vulcan XC-72R) was supplied by Cabot Corporation. Ethanol was purchased from RCI, and potassium hydroxide (KOH) was purchased from Ajex.HNO_3 and H_2SO_4 were purchased from J.T. Backer and Merck, respectively.

2.2 Functionalisation of Carbon Supports

Firstly, 1 g of carbon support (either Vulcan XC-72R or MWCNTs) was mixed with 50 ml of a mixed concentrated H_2SO_4:HNO_3 (3:1) solution in a closed vessel under sonication, at room temperature for 2 hr. After that, the reaction was left undisturbed for another 15 hr. The suspension was washed with deionised water until the effluent had a pH of 4–5. Finally, the treated support was dried in a convection oven at 100°C overnight.

2.3 Physical Characterisation of Carbon Supports

Characterisation of surface area and characterisation of pore size distribution of different carbon supports were carried out by TPR analysis (BELCAT-B). The sample was initially degassed at 300°C for 2 hr in vacuum prior to the N_2 adsorption measurement. Raman spectroscopy (Renishaw Raman Spectrocopy System 2000) was used to investigate the resulting chemical structure and the defects of the carbon supports after functionalisation. Raman spectra were obtained at ambient temperature with a green laser wavelength of 532 nm, radiated from an Argon laser with the power of 2 mW. In addition, FT-IR (Thermo nicolet 6700) was used to diagnose the functional groups obtained from the functionalisation. Each sample was mixed with KBr and was then analysed at wave numbers of 400 to 4000 cm^{-1}. In order to analyse the quantity of functional groups on the supports, TGA (Mettler Toledo TGA/SDTA 851^{e}) was performed at scanned temperatures from 70 to 850 °C, at a ramp rate of 5 °C min^{-1}, and under air flow conditions. Brauner, Emmet and Teller (BET) surface areawas also investigated using Autosorp-I to find specific surface areas of the prepared supports. The samples were degassed at 300 ^{o}C for 2 hr in vacuum before the nitrogen adsorption measurement. Finally, SEM-EDX (FEI Quanta 400 & EDAX) was employed to assess the surface morphology and elemental compositions of supports.

2.4 Catalyst Preparation

The 20%Pd10%Ni10%Sn by weight was prepared from the metal precursors–$PdCl_2$, $NiCl_2$ and $SnCl_2$–on carbon supports. Firstly, the metal precursors were added to deionised water and vigorously stirred. One gram of carbon support was then suspended in the precursor solution for 5 min using a sonicator. After that, an excessive amount of $NaBH_4$ solution was added under vigorous stirring for 6 hr. The mixture was then centrifuged and washed with deionised water several times. The ternary catalyst impregnated on the carbon support was finally dried in a convection oven at 70°C for 20 hr. This method was applied to all types of prepared catalysts [13].

2.5 Physical and Chemical Characterisation of Catalyst Impregnated on Carbon Support

Firstly, XRD (Philips X' pert) was used to investigate the crystallization and phase of catalysts. The XRD patterns were obtained using a Cu K_α source operating at 45 kV and 30 mA with a scan rate of 0.04° s^{-1}. Additionally, TEM (JEOL 2010) was used to investigate the particle size and the dispersion of catalyst particles by the LaB_6 filament at 200 kV. SEM and EDX were also employed to find the morphology of catalyst surface and metal loading ratio, respectively. The form of resulting ternary catalyst was determined using XPS (*AXIS* Ultra DLD) operating in the lens-defined mode swept for 3 times, at a pass energy of 20 eV, a maximum X-ray source power of 150 W, and an energy step size of 100 meV. A gas sorption chemisorption analyser was employed to perform TPR and CO pulsing analysis. The starting and ending temperatures of hydrogen reduction were firstly defined by TPR analysis using 5% H_2 in Argon media at a controlled flow rate of 50 ml s^{-1} and at a wide range of temperatures (from 0 to 650°C). Next, the CO-pulse method was used to provide the number of active sites and metal dispersion. The CO-pulse steps include the following: (i) preheating at 400°C for 25 min, (ii) oxidation with 99.999% O_2 for 15 min, (iii) purging with He for 15 min, (iv) reduction with pure H_2 gas for 15 min, (v) purging with He for 15 min, (vi) cooling to 50 °C, and (vii) injection of 0.89 ml of 10% CO-He until the change in adsorption peaks was below 2%.

2.6 Electrochemical Characterisation of Catalyst Impregnated on Carbon Support

The electrochemical properties of 20%Pd10%Ni10%Sn impregnated on different carbon supports were investigated using a potentiostat and galvanostat(Autolab PGSTAT100) to perform the following measurements: catalytic activity, durability, CO tolerance, and electrochemical surface area. All the measurements employed a three-electrode system operating at room temperature. For the characterisation of catalytic activity, cyclic voltammetry (CV) was carried out in a mixture of 1 M ethanol and 1 M sodium hydroxide aqueous solution. The working electrodes (WEs) were composed of 20%Pd10%Ni10%Sn impregnated on different carbon supports coated on a gas diffusion layer (Toray Carbon Paper, TGP-H-60) with an active surface area of 0.28 cm^2 (Pd metal loading 0.0680 mg cm^{-2}). In the process of WE fabrication, the catalyst ink was prepared from 5 mg of catalyst powder mixed with 1 ml of 5% wt Nafion®117 solution and 1 ml of 5 M ethanol solution. The ink was sonicated for 1 hr to provide a homogeneous suspension. The resulting catalyst ink was deposited on the Toray carbon paper and subsequently dried at 60°C for 10 min. Ag/AgCl and Pt rods were used as a reference electrode (RE) and a counter electrode (CE), respectively. The potential across the WE and the CE was scanned from –0.75 to 0.25 V.

The durability of the prepared catalyst was tested in a mixture of 1 M KOH and 1 M ethanol solution using chronoampermetry (CA). A potential of –0.3 V was constantly applied to the three-electrode system for 1000 seconds, with an active surface area the same as that in the activity test. The electrochemical surface area was analysed from a cyclic voltammogram recorded from –1.2 to 0.5 V at a scan rate of 100 mV s^{-1}, in 1 M KOH solution purging with nitrogen gas with an active surface area of 0.40 cm^2 (Pd metal loading 0.0952 mg cm^{-2}). The method for measuring CO tolerance was rather similar to that of electrochemical surface area. Initially, the CO adsorption on the ternary catalyst system was performed in 1 M KOH solution using CA under CO feeding conditionswith an active surface area the same as that in the ESA test. After that, the electrolyte solution was purged with nitrogen gas to remove all the remaining dissolved CO gas. Finally the potential was scanned from –1.2 to 0.5 V (at 100 mV s^{-1}) to remove the pre-adsorbed CO molecules from the catalyst surface.

3 Results and Discussion

The acid-treated carbon supports and the ternary catalysts were characterised by several methods to assess their suitability for use in DEFCs. The characterisation of carbon supports are detailed in the first subsection. The physical, chemical, and electrochemical characterisations of the catalyst are later explained in more detail in section 3.2.

3.1 Functionalisation of Carbon-Based Supports

The acid functionalisation is known to be a process of removing impurities and inserting acid functional groups on the surface of carbon supports. The hydroxyl group (-OH) of carbon supports was replaced herein by carboxylic group (-COOH) [40, 41]. **Fig. S1** showed the SEM images of CB and MWCNTs before and after functionalisation. The modified surface can be observed to be a rougher surface when compared to the non-functionalised ones. Additionally, the particle sizes of both CB_{sn} and $MWCNT_{sn}$ were found to be decrease after the acid functionalisation. This may be due to residues or impurities being removed from the surface supports.

TGA results are shown in **Fig. S2**. It can be seen that both functionalised supports started to decompose at a lower temperature when compared to the non-functionalised ones (i.e., untreated samples). This indicated that the existence of acid functional groups in the supports caused a decrease in the thermal stability of the supports. The weight loss of those functionalised supports was located at approximately 230 °C, a temperature associated with the decomposition of carboxylic groups [39]. It was also found that the decomposition temperature of $MWCNT_{sn}$ was higher than that of CB_{sn}. The decomposition temperature of carbon-based supports was in the range of 400–700 °C. The residues obtained at the end of

TGA measurement indicated the impurity level of the samples [39]. After the thermal decomposition, both functionalised supports contained less residue than that contained on the non-functionalised ones. This can imply that the acid functionalisation helped to remove some impurities despite causing the reduction of thermal stability. The weight percents of acid functional groups were 5.85% and 5.42% for CB_{sn} and $MWCNT_{sn}$, respectively.

Raman spectroscopy was used to verify the existence of -COOH functional groups with the change of bond structure among the functionalised carbon supports. **Fig. S3** shows Raman spectra of all carbon supports. D band at 1350 cm^{-1} appeared as a shoulder to G band (located at around 1580-1620 cm^{-1}). It was suggested that the D band originated from hybridised vibration associated with graphene edges, which usually indicates the presence of disorder in the graphene structure. The high intensity of D band in carbon materials referred to a higher order of defects or disorder in the graphene structure. The high intensity of G band indicated less carbon amorphous and high crystalline structures of the untreated MWCNTs. G’ band (the overtone of D band at 2D position) corresponding to the stacking order of the graphitic walls and the crystalline of the graphitic planes [42-44]. The ratios of D band and G band intensity (I_D/I_G) of all supports are given in **Table S1**. The I_D/I_G ratio of $MWCNT_{sn}$ was higher than that of MWCNTs as a result of covalent functionalization of the MWCNT sidewall being increased after acid treatment [45]. However, the I_D/I_G ratio of CB_{sn} was slightly lower than that of CB, indicating that the degree of disorder of the microcrystalline structure of CB was not as badly effected as that of MWCNTs by acid treatment [33].

FTIR was used to confirm the functional groups attached to the original structures. The stretching and bending vibrations of atoms were used to determine the functional groups in the structures. As explained previously, the acid treatment enabled the purification and/or functionalisation of carbon supports to occur. The process was related to the oxidation of the double bond in graphene wall yielding sulfonated group (SO_3), carboxylic groups (COOH), and hydroxyl groups (OH) on the carbon surface [46, 47]. **Fig. 1** shows FTIR spectra of all carbon supports. It can be seen that characteristic peaks of CB_{sn} and $MWCNT_{sn}$ were located at the same position, but the peak intensity of CB_{sn} was weaker than that of $MWCNT_{sn}$. The fingerprint region below 1400 cm^{-1} could hardly be used to identify any compounds because of its complexity. The peaks at around 3400 $cm^{-1}$and at around 1640 cm^{-1} referred to H-bond of hydroxyl groups and H-bond of carboxyl groups (C=O), respectively. These H-bonds were conjugated with C=C bonds (i.e., at approximately 1600 cm^{-1}) in the graphene wall of $MWCNT_{sn}$ [48]. In addition, the peaks at approximately 2900 cm^{-1} and 620 cm^{-1} corresponding to C-H bond were also obtained. It was believed to undergo oxidation reaction due to the presence of C-O bonds at approximately 1475 cm^{-1}. Moreover, the peak at around 1100 cm^{-1} can be observed, indicating the formation of sulfonated groups and corresponding to C-O vibration [49].

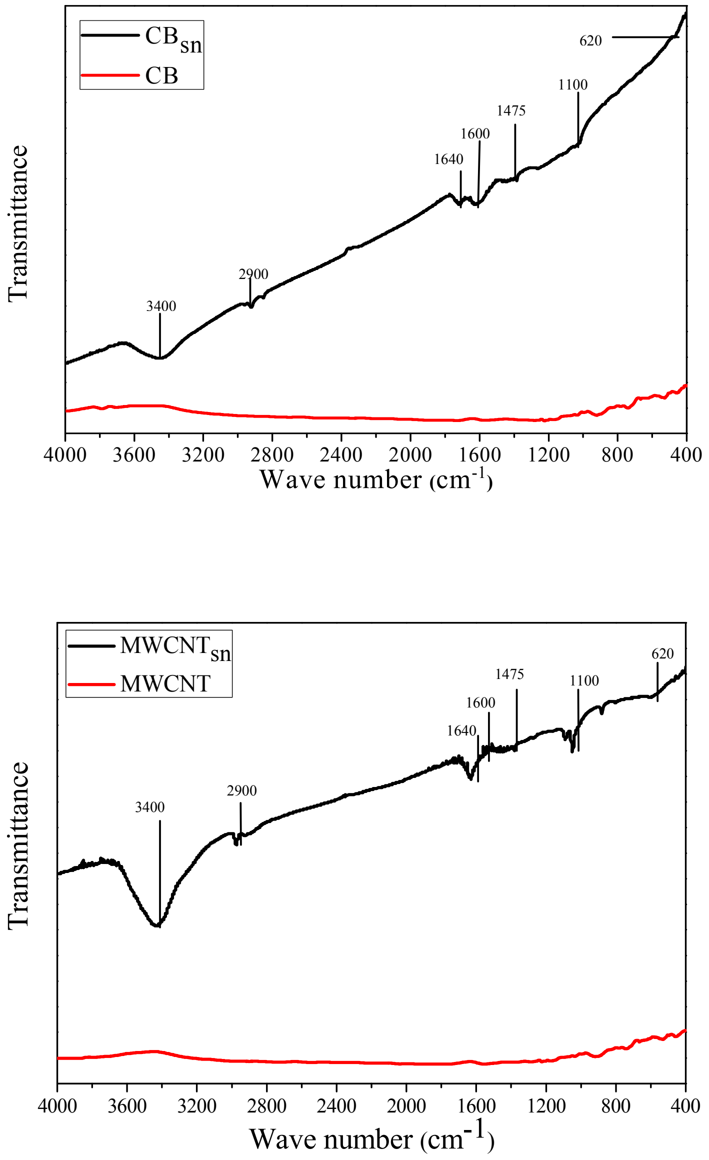

Fig. 1 The FT-IR spectra of CB compared with CB$_{sn}$ (top) and MWCNTs compared with MWCNT$_{sn}$ (bottom) revealing the effect of acid functionalisation.

The specific surface areas of supports strongly affected the activity of catalyst. The multilayer adsorption model or BET method was used to analyse the surface area of the supports. According to IUPAC isotherms, all the support samples showed type-II adsorption isotherms, a normal form of isotherms shown by a finely divided non-porous adsorbent. This represents an unrestricted monolayer-multilayer adsorption [50]. The conversion of the isotherm graph to BET graph resulted in a linear relationship between $1/W[(P/P_0)-1]$ and P/P_0, as shown in **Fig. S4**.

Fig. S4 reveals an increase in the slopes of the functionalised supports when compared to the non-functionalised ones. This means that the surface area of the functionalised supports was greatly higher than that of the non-functionalised supports. The values of BET surface area (S_{BET}) were calculated as given in **Table S2**. The S_{BET} values of the CB and MWCNTs were 427.4 and 221 m^2/g, respectively agree very well with the values reported in the literature [51, 52]. The S_{BET} of the pore diameters for all samples were below 250 Å or 25 nm, indicating the formation of mesopores. Interestingly, the S_{BET} values of $MWCNT_{sn}$ and CB_{sn}decreased by 42% and 62%, respectively, which was also observed by Paulina *et al.* (2012). The BET surface area of the two functionalised carbon supports decreased due to the increasing functional group content. This can be related to the blocking of the inter-bundle galleries and intra-bundle interstitial channels by the functional groups[53].

3.2 Properties of Electrocatalysts on Different Carbon Supports

3.2.1 Physical Properties

20%Pd10%Ni10%Sn was impregnated on four different carbon supports: CB, CB_{sn}, MWCNTs, and $MWCNT_{sn}$. The selected catalyst composition showed the maximum current density for EOR as reported in our previous study [54]. The physical properties of 20%Pd10%Ni10%Sn deposited on different carbon supports were analysed using XRD, SEM-EDX, TEM, CO-pulse chemisorptions, and XPS. Then, the electrochemical properties were characterised using a potentiostat/galvanostatto explorethe activity, durability, CO tolerance and electrochemical surface area (ESA) of those samples.

XRD was used to identify the forms of metal catalysts as demonstrated in **Fig. 2**. All catalysts revealed similar peak positions, indicating the identical forms of metal catalysts deposited on different supports. The first peak at around 25–30° was (0 0 2) plane of carbon structure in CB or MWCNTs. The characteristic peaks of Pd included the peaks at 39.901°, 46.209°, 67.618°, 81.364°, and 86.342°, which referred to (1 1 1), (2 0 0), (2 2 0), (3 1 1), and (2 2 2) planes, respectively. All peaks of Pd represented face-centred cubic (FCC) structure. The peaks at 33.193° and 59.303° referred to (1 0 0) and (1 1 0) planes of Ni(OH)$_2$, respectively, whereas the peaks at26.511°, 33.769°, 51.612°, and 65.752° referred to (1 1 0), (1 0 1), (2 1 1), and (3 0 1) planes of SnO$_2$, respectively. The SnO$_2$ peaks were difficult to observe as three peaks of SnO$_2$ were overlapped with the peaks of amorphous carbon (25-30°), Ni(OH)$_2$ (33.193°), and Pd (67.618°).

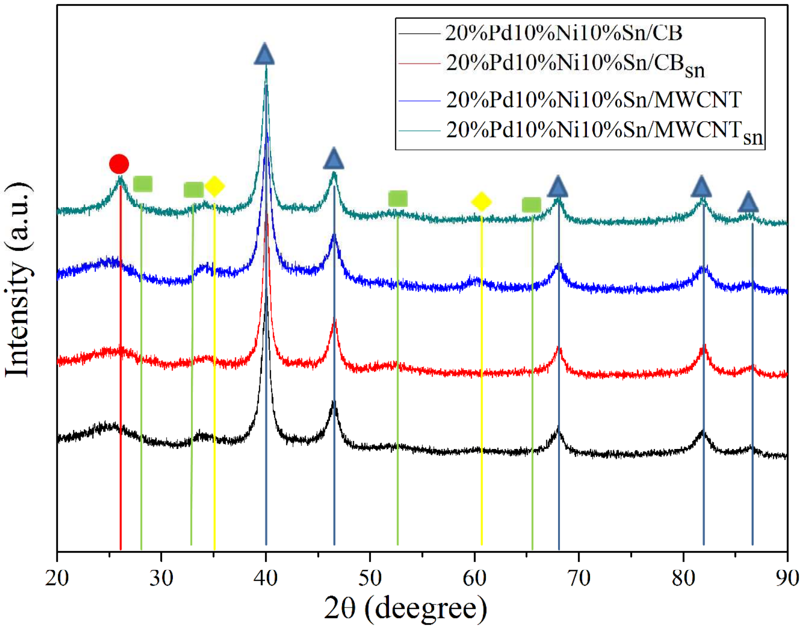

Fig. 2 XRD patterns of all prepared catalysts at 2θ =20-90° (●Carbon ◆Ni(OH)$_2$🟩SnO$_2$▲ Pd).

The peak of Pd (2 2 0) at 67.618° was used to calculate spacing, lattice parameter, and crystalline size in all samples. The lattice parameter is the physical dimension of unit cells in a crystal lattice, and d-spacing is the spacing between the planes. The results are given in **Table 1**. It was found that the crystalline size of catalysts was in the range of 6.4–7.4 nm, and similar values of d-spacing and lattice parameter were obtained.

Table I D-spacing, lattice parameter, and crystalline size calculated from the Pd peak at (2 2 0) plane

Composition	2θ	D-spacing (nm)	Lattice parameter (nm)	Crystalline size (nm)
20%Pd10%Ni10%Sn/CB	67.845	0.13802	0.39038	6.8
20%Pd10%Ni10%Sn/CB_{sn}	67.911	0.13791	0.39007	6.6
20%Pd10%Ni10%Sn/MWCNT	67.916	0.13790	0.39004	6.4
20%Pd10%Ni10%Sn/$MWCNT_{sn}$	67.813	0.13808	0.39054	7.4

SEM images of all samples are demonstrated in **Fig. 3**. The metal particles were dispersed uniformly on the surface of carbon supports. The actual compositions of as-prepared catalyst samples were examined using SEM-EDX with 5 sampling points per sample. It was found that the actual compositions were quite similar to the desired compositions as shown in **Table 2.**

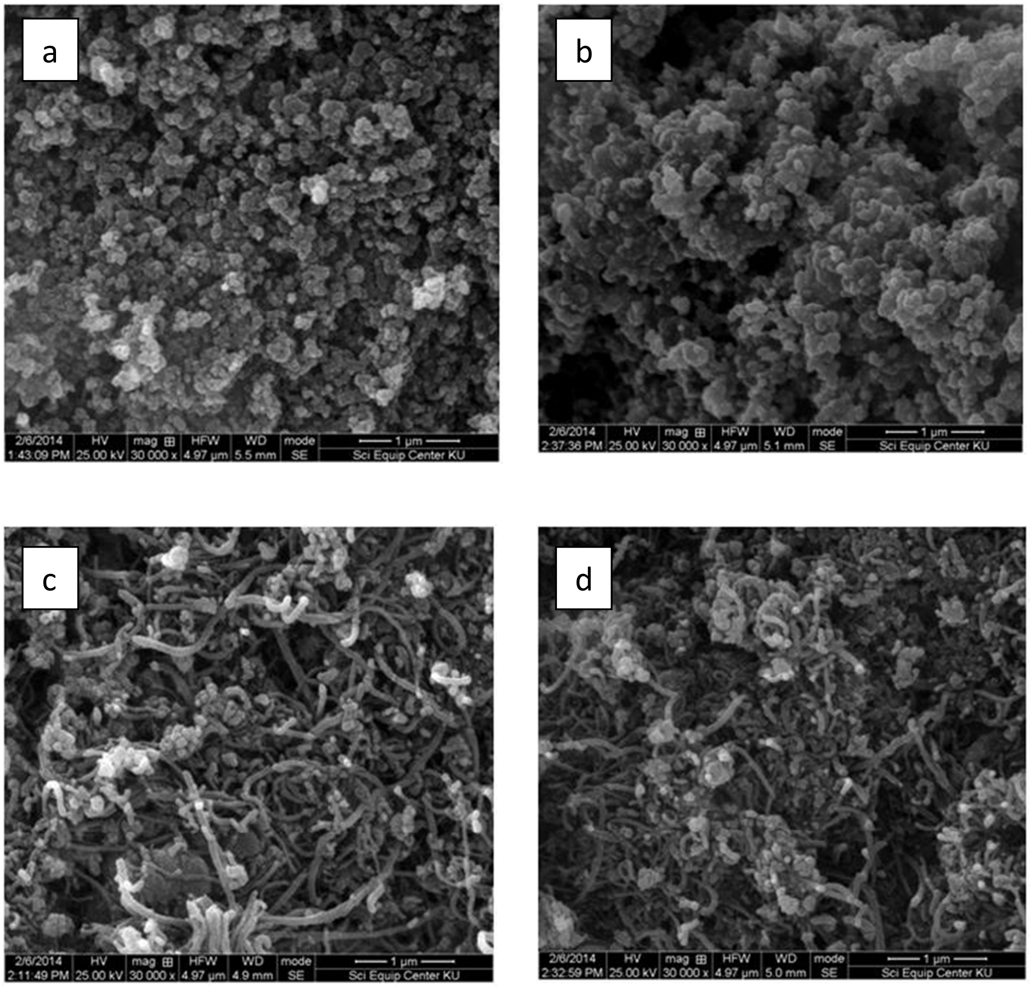

Fig. 3 SEM images (×30,000) of 20%Pd10%Ni10%Sn catalyst on (a) CB, (b) CB_{sn}, (c) MWCNTs, and (d) $MWCNT_{sn}$.

Table II Elemental compositions of 20%Pd10%Ni10%Sn catalyst ondifferent carbon supports.

Catalyst/Carbon support	Desired composition (% wt)			Actual composition using EDX (% wt)		
	Pd	Ni	Sn	Pd	Ni	Sn
20%Pd10%Ni10%Sn/CB	50	25	25	49.21±2.92	23.58±5.45	27.22±2.58
20%Pd10%Ni10%Sn/CB$_{sn}$	50	25	25	52.11±4.69	16.45±2.00	31.44±3.34
20%Pd10%Ni10%Sn-/MWCNT	50	25	25	53.78±3.99	16.81±2.38	29.41±2.09
20%Pd10%Ni10%Sn/MWCNT$_{sn}$	50	25	25	45.37±6.47	29.25±6.33	25.37±1.83

TEM images of 20%Pd10%Ni10%Sn on various supports (in **Fig. 4**) show that metal catalysts were well dispersed on all carbon supports. The histograms of catalyst particle size distribution on various supports (in **Fig. 5**) reveal a narrow average particle size of 6.0–6.7 nm. The catalyst particle sizes larger than 14 nm shown in **Fig. 5** may come from the overlapping of the supports was not averaged.

The metal dispersion (D_m) and the number of active sites (N_s) of 20%Pd10%Ni10%Sn on various supports assessed by chemisorption are given in **Table 3.** It was found that the catalyst on both MWCNT$_{sn}$ and CB$_{sn}$ exhibited high levels of D_m and N_s implies that well-dispersed and distributed metal particles were achieved with the use of acid functionalised carbon supports. The D_m result was consistent with the catalyst distribution results observed by TEM.

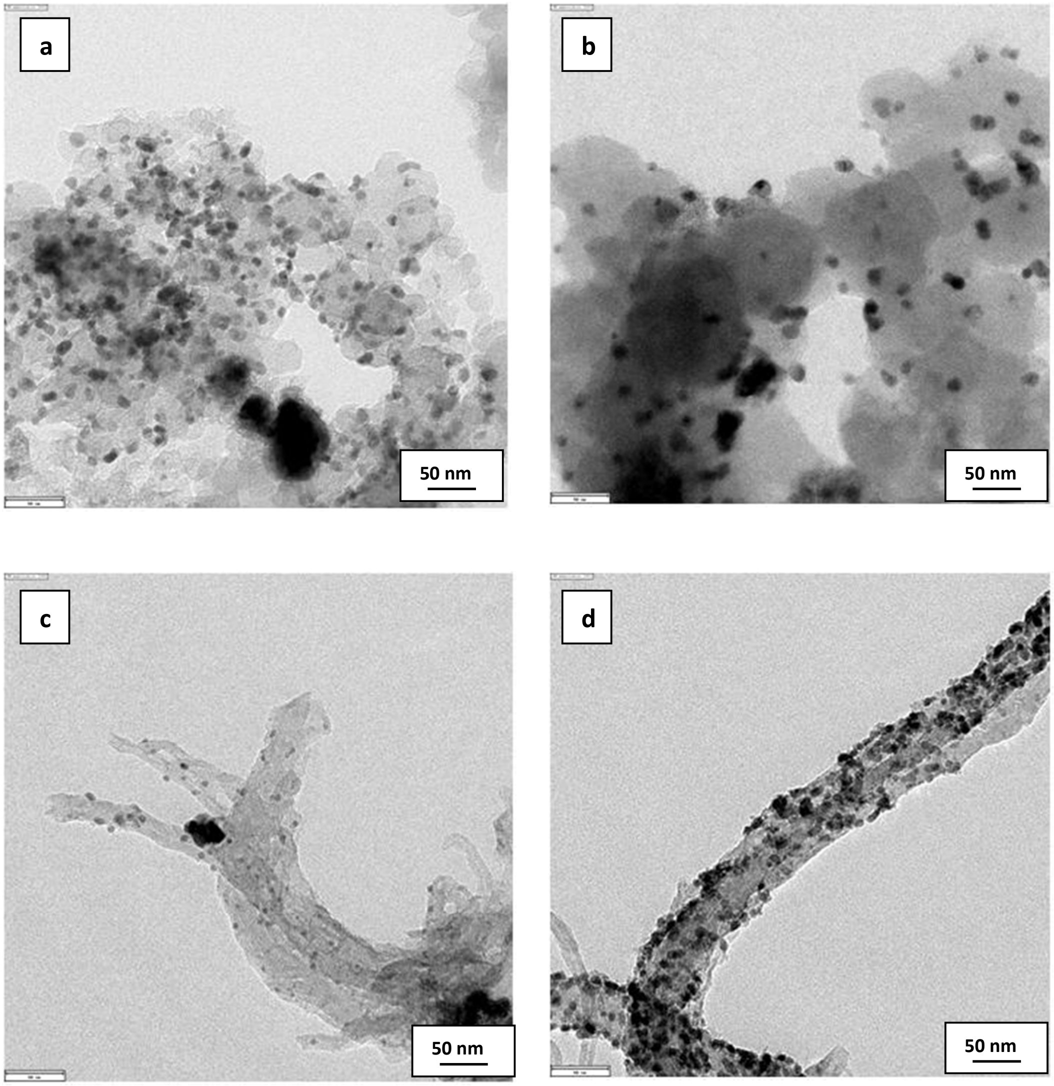

Fig. 4 TEM images at (×50,000) of 20%Pd10%Ni10%Sn catalyst on (a) CB, (b) CB_{sn}, (c) MWCNTs, and (d) $MWCNT_{sn}$.

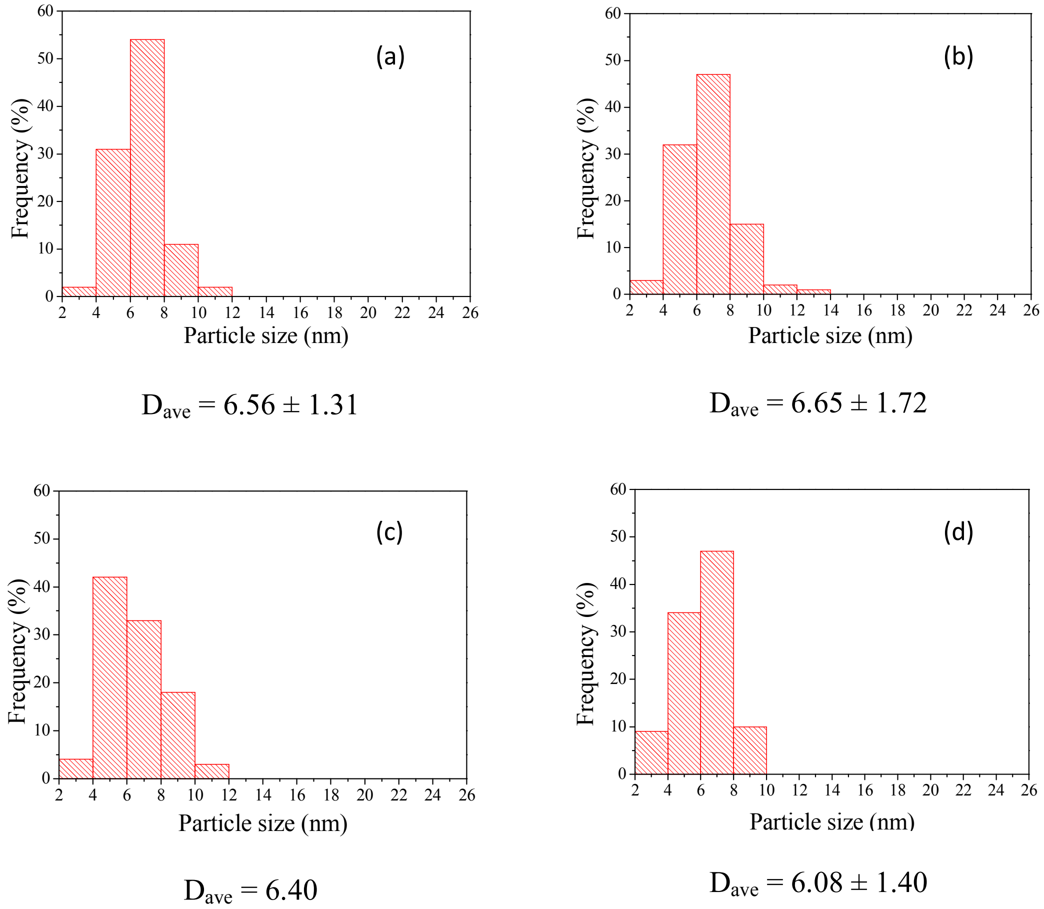

$D_{ave} = 6.56 \pm 1.31$

$D_{ave} = 6.65 \pm 1.72$

$D_{ave} = 6.40$

$D_{ave} = 6.08 \pm 1.40$

Fig. 5 Particle size distribution of 20%Pd10%Ni10%Sn catalyst on (a) CB, (b) CB_{sn}, (c) MWCNTs, and (d) $MWCNT_{sn}$.

Table III Metal dispersion (D_m) and number of active sites (N_s) of 20%Pd10%Ni10%Sn on different carbon supports.

Catalyst	D_m (%)	N_s (site)
20%Pd10%Ni10%Sn/CB	1.4474	1.64E+19
20%Pd10%Ni10%Sn/CB_{sn}	2.1705	2.46E+19
20%Pd10%Ni10%Sn/MWCNT	0.9251	1.05E+19
20%Pd10%Ni0%Sn/$MWCNT_{sn}$	2.8822	3.26E+19

XPS was carried out to evaluate the oxidation number of metal catalysts. **Fig. 6a** show the XPS survey scanned of 20%Pd10%Ni10%Sn catalyst on CB_{sn} and $MWCNT_{sn}$ supports. The survey scan contained the atomic peaks of carbon (C 1s), oxygen (O 1s), nickel (Ni 2p), tin (Sn 3d), and palladium (Pd 3d). The XPS area ratios of chemical state of Pd, Ni and Sn species and their oxidation states are detailed in **Table 4**. The XPS spectrum of Pd 3d peak consisted of two dominant peaks and three sub-peaks, corresponding to Pd metal (Pd^0) and PdO (Pd^{2+}) forms, respectively. The XPS spectrum of Ni 2p peak was composed of two dominant peaks and four sub-peaks associated to Ni, NiO, $Ni(OH)_2$, and NiOOH with the oxidation states of Ni^0, Ni^{2+}, Ni^{2+}, and Ni^{3+}, respectively. The XPS spectrum of Sn 3d included two main peaks and three sub-peaks associated to Sn-SnO and SnO_2 withthe oxidation states of Sn^0-Sn^{2+} and Sn^{4+}, respectively. In both catalyst samples, the highest ratios of $Ni(OH)_2$ and SnO_2, which are known to promote the EOR and CO oxidation, respectively, were obtained [11, 13, 17, 18]. **Fig. 6b**, **Fig. 6c**, and **Fig. 6d** show XPS spectra of Pd 3d, Ni 2p, and Sn 3d, respectively, of catalyst on $MWCNT_{sn}$ (top) and MWCNT (bottom). The carbon support showed the interaction between metal loading by the shift of metal peak. The XPS results show a positive shift of 0.1 eV for Pd 3d and a negative shift 0.4 eV for Sn 3d on catalyst on MWCNTsn [55, 56]. In the case of Ni on MWCNT, the peak contained much noise and was of a low intensity making it hard to identify the position of peak for the peak shift.

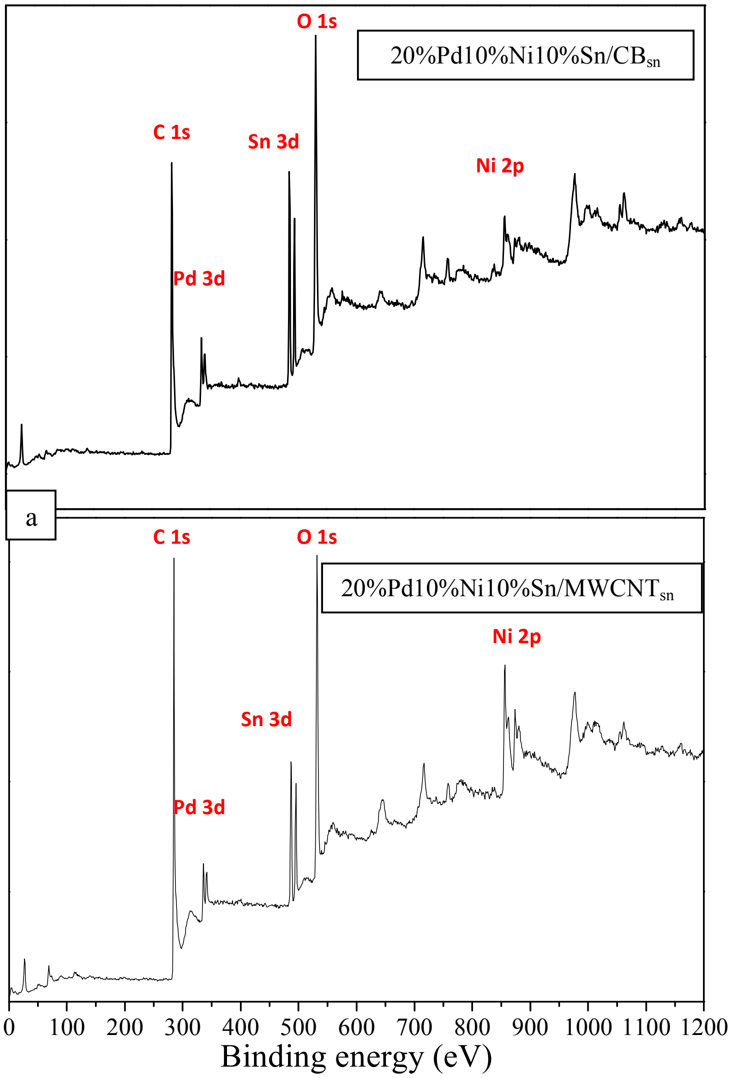
O 1s
20%Pd10%Ni10%Sn/CB$_{sn}$
C 1s
Sn 3d
Ni 2p
Pd 3d
a
C 1s
O 1s
20%Pd10%Ni10%Sn/MWCNT$_{sn}$
Ni 2p
Sn 3d
Pd 3d
0
100
200
300
400
500
600
700
800
900
1000
1100
1200
Binding energy (eV)

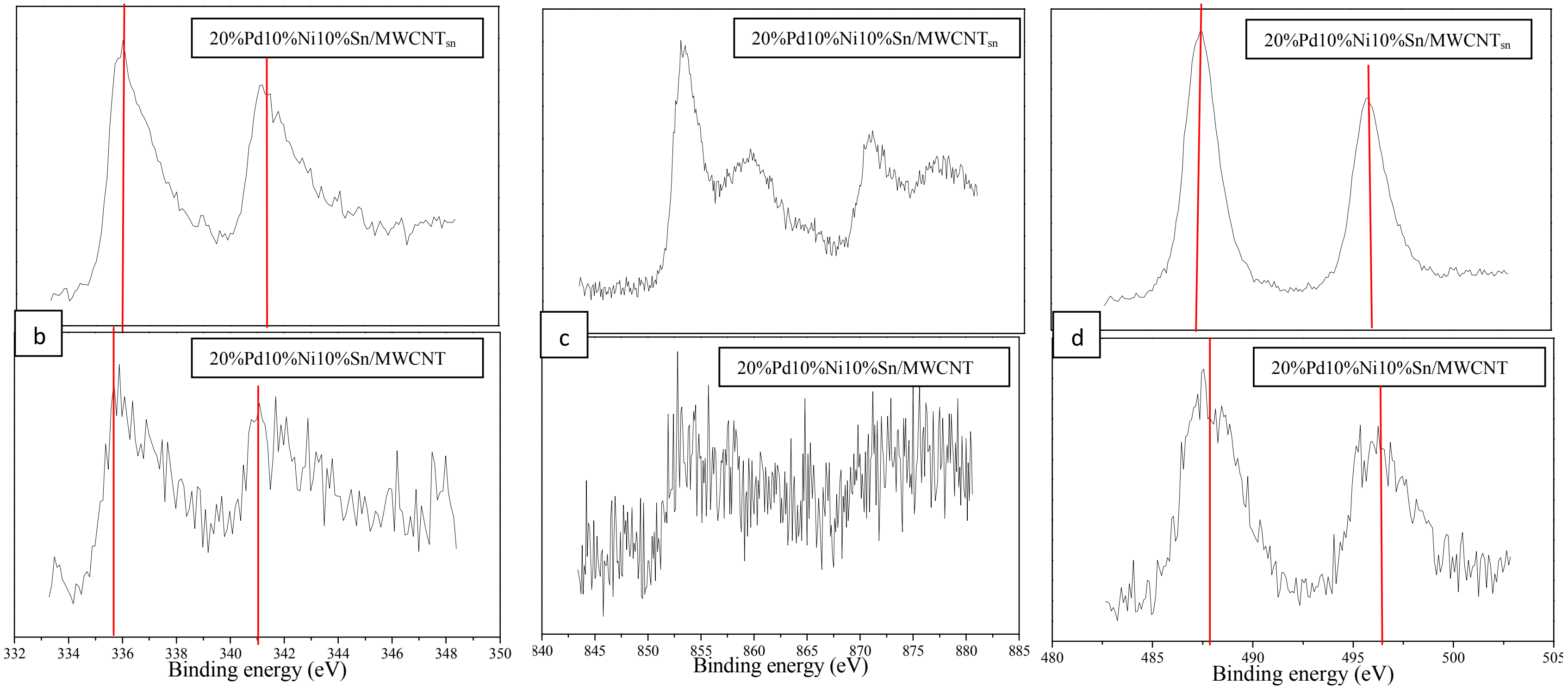

Fig. 6 (a) Survey XPS spectra of 20%Pd10%Ni10%Sn on CB$_{sn}$ and MWCNT$_{sn}$; (b) XPS spectra of Pd 3d of catalyst on MWCNT$_{sn}$ and MWCNT; (c) XPS spectra of Ni 2p of catalyst on MWCNT$_{sn}$ and MWCNT; (d) XPS spectra of Sn 3d of catalyst on MWCNT$_{sn}$ and MWCNT.

Table IV XPS area ratios of chemical state of Pd, Ni, and Sn species.

Form of metal	XPS area ratio (%)	
	Metal on CB_{sn}	Metal on $MWCNT_{sn}$
Pd (0)	87.5	12.5
PdO (2+)	87.5	12.5
Ni (0)	9.0	5.7
NiO (2+)	15.3	9.2
$Ni(OH)_2$ (2+)	60.0	51.8
NiOOH (3+)	15.7	33.3
Sn-SnO (0,2+)	4.5	95.5
SnO_2 (4+)	3.3	96.7

3.2.2 Activity, Stability, CO Tolerance, and Electrochemical Surface Area (ESA)

The cyclic voltammograms of the catalyst samplesfor EOR were recorded in a mixture of 1 M ethanol and 1 M KOH aqueous solution and are shown in **Fig.7.** The EOR can be observed on the anodic peak which was located between –0.2 and 0.1 V. It can be seen that the onset potentials were relatively similar for all samples. **Table 5** shows the corresponding anodic peak potentials and current densities for EOR. The 20%Pd10%Ni10%Sn/MWCNT$_{sn}$ exhibited the maximum current density or activity (291 mA cm^{-2}) and mass activity (4288 mA mg$_{Pd}^{-1}$). It has been suggested that the catalytic activity towards EOR was more favourable when the catalyst exhibited a higher magnitude of anodic current density but a lower value of the onset potential [57]. Comparing to other works, it was found that the catalyst activity Pd_2Ni_3/C prepared byShen*et al*. showed lower current density (about 80 mA cm^{-2}) and the Pd/C catalyst prepared by Yi *et al*. also showed a current density about 50% lower than that obtained with catalysts prepared in this work [13, 57]. The highest mass activity of the catalyst on MWCNT$_{sn}$ (about 2–3 times that of others) suggested that Pd supported on MWCNT$_{sn}$ plays a more effective utility value [9]. The results also confirmed that the 20%Pd10%Ni10%Sn deposited on functionalised supports generated higher current density than those on non-functionalised supports. This may be due to high crystallinity and strongly covalent bondof support, leading to a good dispersion and a nanoparticle size of metal [58, 59]. In terms of catalyst activity, MWCNT$_{sn}$ was found to be a promising catalyst support for EOR in DEFC.

The stability of 20%Pd10%Ni10%Sn catalyst deposited on different carbon supports was determined by chronoamperometry. The test method reported by Yaojuan *et al.* and Changwei *et al.* was followed [60, 61].The stability was found unchanged after 1000 s. Therefore, the stability test of catalyst was carried out and the results are demonstrated in **Fig. 8**. The percentage of current drops of MWCNT$_{sn}$, MWCNT, CB, and CB$_{sn}$ were 2.58, 1.15, 0.76, and 0%, respectively. Thus, 20%Pd10%Ni10%Sn/MWCNT$_{sn}$ exhibited the greatest catalyst stability. The reason for that was because the covalent bonds of carboxylic functional groups attached to the MWCNT$_{sn}$ surface enabled a good interaction among metals and support [58] and the high degree of crystallinity of the MWCNT$_{sn}$ support resulted in a good electrical connection in molecular level [62].

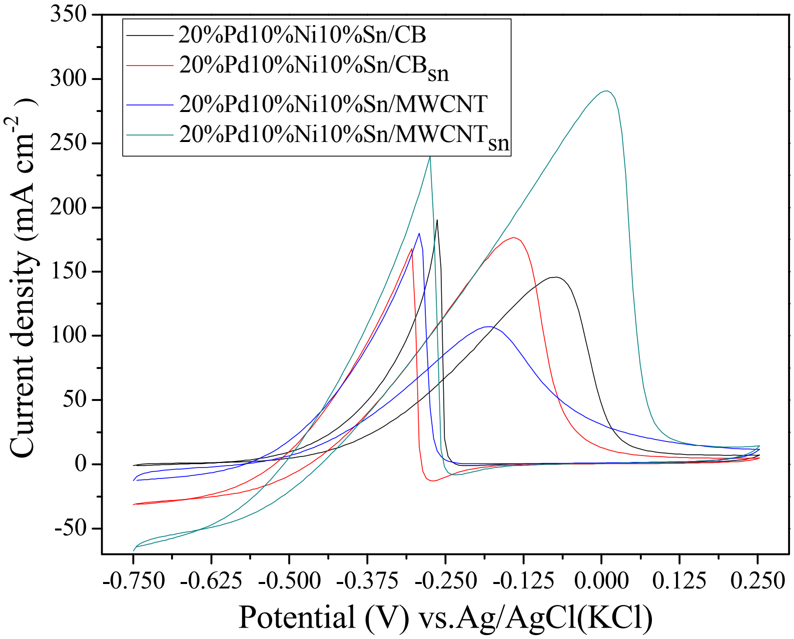

Fig. 7 Voltammograms of 20%Pd10%Ni10%Sn deposited on different catalyst supports recorded in a mixture of 1 EOH and 1 M KOH at a scan rate of 50 mA s^{-1}.

Table V The data extracted from cyclic voltammograms (Figure 11) of20%Pd10%Ni10%Sn deposited on different catalyst supports recorded in a mixture of 1MeOH and 1 M KOH.

	Cyclic voltammetry of ethanol oxidation				CO-stripping		ESA	
Catalyst on	Onset potential (V)	Anodic peak voltage (V)	Anodic peak current density or activity (mA cm^{-2})	Mass activity (mA mg$_{Pd}^{-1}$)	CO stripping onset potential (V)	CO stripping peak potential (V)	Area of desorbed OH$^-$ peak (mC cm^{-2})	ESA (m^2 g^{-1}Pd)
CB	-0.414	-0.077	146	2151	-0.478	-0.162	22.856	59.255
CB$_{sn}$	-0.419	-0.141	177	2608	-0.480	-0.168	23.791	61.680
MWCNT	-0.472	-0.182	107	1576	-0.415	-0.174	19.711	52.615
MWCNT$_{sn}$	-0.396	0.096	291	4288	-0.368	-0.179	29.760	77.155

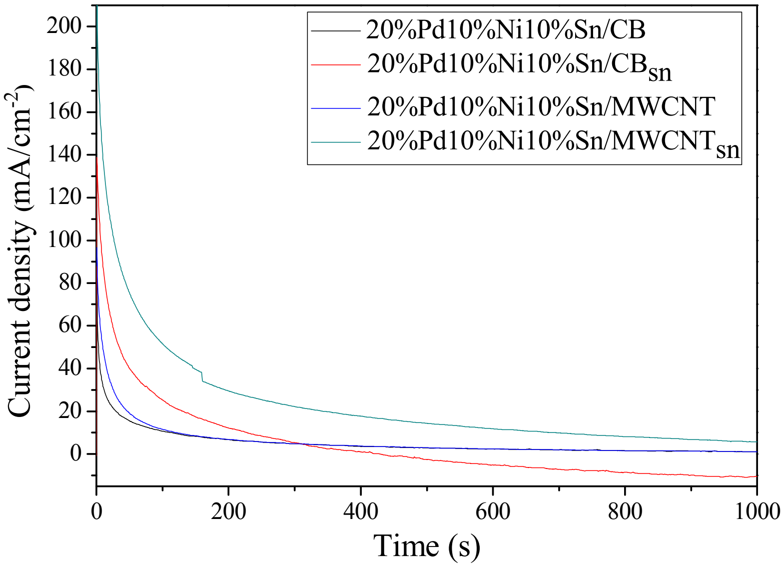

Fig. 8 Chronoamperometric curves of 20%Pd10%Ni10%Sn deposited on different catalyst supports recorded in a mixture of 1 M ethanol and 1 M KOH solution at an applied potential of –0.3 V.

A CO-stripping test was also used to indicate the catalyst ability in the presence of CO poisoning in the system. It is also a useful method for determination of electrochemical surface area, especially for Pd-based catalysts. CO-stripping voltammograms of 20%Pd10%Sn10%Ni on various supports are demonstrated in **Fig.9**; the inset shows the onset potential and the peak potentialfor CO oxidation. The peak for CO oxidation occurred at around –0.1 to –0.2 V with the onset potential in a range of –0.368 to –0.480 V. The metal promoters (Sn and Ni) facilitated the removal of CO poison on Pd surface and the refreshing of reaction sites for ethanol oxidation. As regards to the onset potential of CO oxidation peak, a lower value indicates well facilitated CO removal on Pd surface for the route of ethanol oxidation. The catalyst on MWCNT and MWCNT$_{sn}$ supports showed lower onset potentials than the catalyst on CB and CB$_{sn}$ supports. This might be due to the better effect of Ni and Sn oxides on the catalyst surface of MWCNT and MWCNT$_{sn}$, or it could be due to the effect of Pd-Ni and Pd-Sn alloys on CO removal reaction [63]. The reaction pathways to remove CO poisoning of metal oxide (MtO$_x$: SnO$_x$, NiO$_x$) are shown in equations (1) –

(3), with the metal oxide forms revealed by XPS and XRD results. Moreover, the catalyst on functionalised support exhibited lower onset potential (the lowest onset potential was the catalyst on $MWCNT_{sn}$) than the non-functionalised one, as showed in **Fig. 9**. The onset and peak potentials for CO-stripping process extracted from **Fig. 9** are detailed in **Table 5.** The peak potential was in the range of –0.162 to –0.179 V. The catalyst on MWCNT and $MWCNT_{sn}$ had lower onset potentials than those ofthe catalyst on CB and CB_{sn}, indicating the higher efficiency for CO tolerance obtained when using MWCNT supports.

$2Pd + CH_3CH_2OH \Rightarrow 2Pd\text{-}CO_{ads} + 6H^+ + 6e^-$ (1)

$MtO_x + H_2O \Rightarrow MtO_x\text{–}OH_{ads} + H^+ + e^-$ (2)

$Pd\text{–}CO_{ads} + MtO_x\text{–}OH_{ads} \Rightarrow Pd + MtO_x + CO_2 + H^+ + e^-$ (3)

where MtO_x is a metal oxide such as SnO_x, NiO_x.

Furthermore, another anodic peak which is associated to Ni metal and, in particular, the oxidation of $Ni(OH)_2$ to NiOOH was found at approximately 0.4–0.5 V. As regards another cathodic peak, it was found that the reduction reaction of NiOOH to $Ni(OH)_2$ was at about 0.4–0.2 V, as shown in equations (4)–(5). These peaks are associated to the increasing of activity of catalyst. Ni metal on the support catalyst can work similarly to Pd (on catalyst activity) and reduce CO- poisoning in the same manner as Sn.

$Ni(OH)_2 + OH^- \leftrightarrow NiOOH + H_2O + e^-$ (4)

$NiOOH + H_2O + e^- \leftrightarrow Ni(OH)_2 + OH^-$ (5)

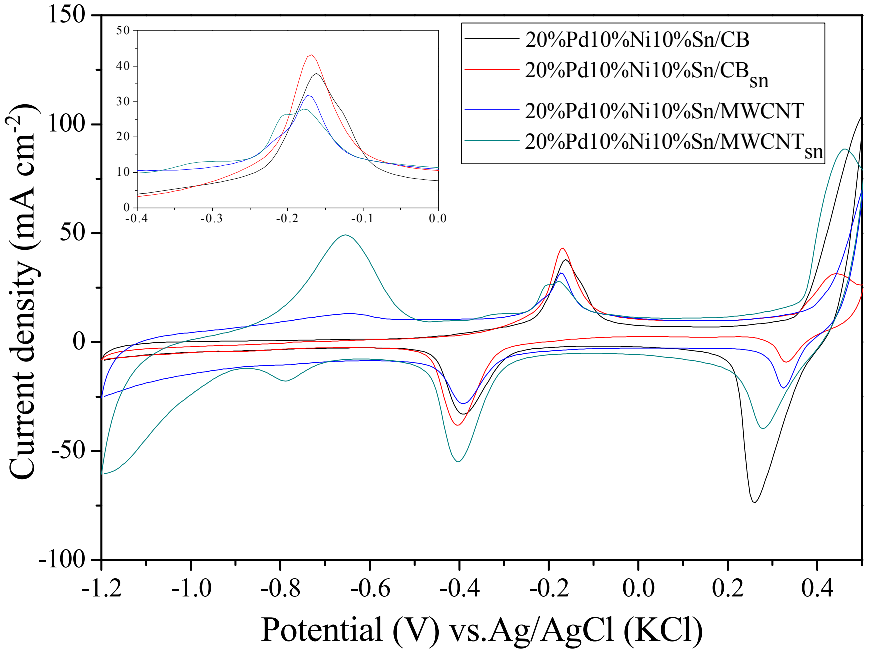

Fig. 9 CO stripping voltammograms of 20%Pd10%Sn10%Ni on various carbon supports and the corresponding forward scan of CO stripping voltammograms (inset).

ESAs of the 20%Pd10%Ni10%Sn on various supports were determined by hydroxyl (OH^-) adsorption in 1 M KOH solution. **Fig. 10** shows the cyclic voltammograms of those catalyst samples. OH^- desorption was used to calculate the ESA values (given in **Table 5**). The anodic peak appeared in the forward scan, and cathodic peak showed in the backward scan. In the forward scan, the oxidation peak was at –0.65 V, associated to the formation of the OH^- group adsorption (OH_{ads}) on the Pd surface which was then converted to Pd-OH_{ads}. After that, the backward scan caused the electrodesorption of the pre-adsorbed OH_{ads} from the Pd surface. In **Table 5** it can be seen that the use of functionalised supports exhibited higher ESAs than those obtained with the non-functionalised supports. $MWCNT_{sn}$ showed the highest ESA which may be due to the metal was well attached to and dispersed in this support. This agreed well with TEM results. Moreover, the result was consistent with the number of active site measured from CO chemisorption test. Among the samples, the $MWCNT_{sn}$ was found to be the most suitable support for the deposition of

20%Pd10%Ni10%Sn as a ternary catalyst in DEFC, as it had excellent catalytic activity and stability, great performance for CO tolerance, and the highest ESA.

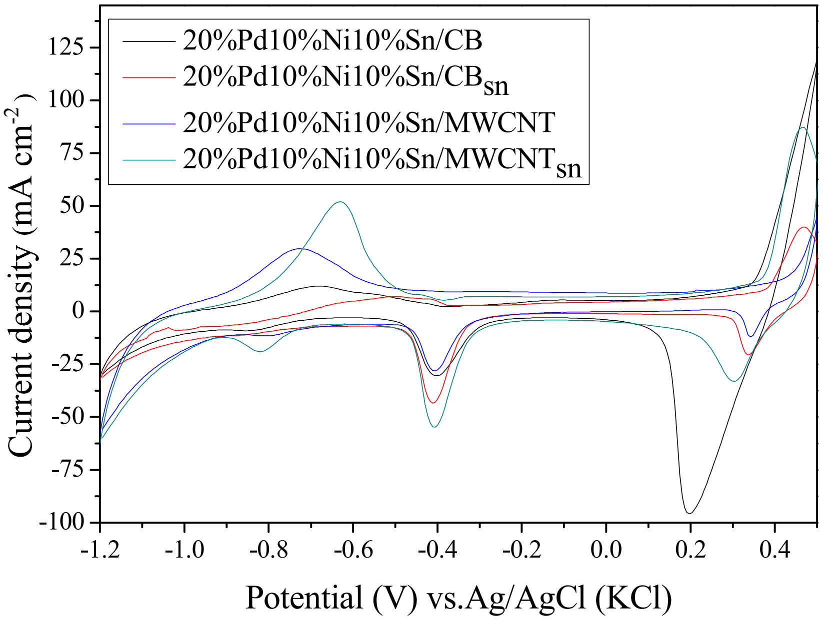

Fig. 10 Cyclic voltammograms of all samples for OH^- adsorption and desorption in 1 M KOH solution.

4 Conclusions

The 20%Pd10%Ni10%Sn tri-metallic electrocatalyst was synthesised on four different carbon supports (i.e., CB, CB_{sn}, MWCNT, and $MWCNT_{sn}$) to investigate the most suitable support for DFECs electrode. The catalyst samples were produced using a $NaBH_4$ reduction method, which is a simple and a versatile technique. Then, their physical and electrochemical properties were characterised using several techniques. The results obtained by TGA diagram, Raman spectra, and FTIR spectra verified the existence of acid functional groups on both functionalised supports: CB_{sn} and $MWCNT_{sn}$. However, TGA and BET results suggested that the thermal stability and S_{BET} were decreased after acid functionalisation. The actual catalyst compositions in all samples were investigated by EDX, and the results agreed very well with the desired composition of 20%Pd10%Ni10%Sn. TEM micrographs demonstrated the narrow size distribution and good dispersion of catalyst particles on the $MWCNT_{sn}$ support with an average particle size of 6.08–6.65

nm. The acid functionalisation was found vis characterisation by CO chemisorption to increase the number of active sites. Moreover, the crystalline forms of Pd, $Ni(OH)_2$, and SnO_2 were confirmed by the XRD and XPS results. For the electrical properties of 20%Pd10%Ni10%Sn deposited on different supports, it was found that the 20%Pd10%Ni10%Sn/$MWCNT_{sn}$ exhibited outstanding electrical properties, including a maximum current density of 291 mA cm^{-2} for EOR, high catalyst stability and ESA, and excellent CO tolerance. This may be due to high crystallinity and strongly covalent bonds of $MWCNT_{sn}$ and the metals, leading to a good dispersion and a nanoparticle of metal.

5 Acknowledgements

This work was financially supported by the Kasetsart University Research and Development Institute (KURDI) and National Metal and Materials Technology Center (P1301014) Thailand.

References

1. C.-T. Hsieh, Y.-Y. Liu, W.-Y. Chen and Y.-H. Hsieh, *International Journal of Hydrogen Energy*, 2011, **36**, 15766-15774.
2. H. David, T. Reginald, B. Steve and J. Amanda, Hydrogen for fuel cell electric vehicles, http://www.renewableenergyfocus.com/blog/2013/9/19/hydrogen-for-fuel-cell-electric-vehicles/1006.aspx, (accessed September 12, 2014, 2014).
3. Y. H. Chu and Y. G. Shul, *International Journal of Hydrogen Energy*, 2010, **35**, 11261-11270.
4. E. Antolini and E. R. Gonzalez, *Journal of Power Sources*, 2010, **195**, 3431-3450.
5. H. T. Roelofs KS, Schiestel T., *Material Science and Engineering*, 2011, **176**, 727-735.
6. Y. Li and Y. He, *RSC Advances*, 2014, **4**, 16879-16884.
7. N. Wongyao, A. Therdthianwong and S. Therdthianwong, *Energy Conversion and Management*, 2011, **52**, 2676-2681.
8. S. Meenakshi, P. Sridhar and S. Pitchumani, *RSC Advances*, 2014, **4**, 44386-44393.
9. R. Wang, J. Yang, K. Shi, B. Wang, L. Wang, G. Tian, B. Bateer, C. Tian, P. Shen and H. Fu, *RSC Advances*, 2013, **3**, 4771-4777.
10. L. An, T. S. Zhao, R. Chen and Q. X. Wu, *Journal of Power Sources*, 2011, **196**, 6219-6222.
11. T. Ramulifho, K. I. Ozoemena, R. M. Modibedi, C. J. Jafta and M. K. Mathe, *Electrochimica Acta*, 2012, **59**, 310-320.
12. H. Liu, C. Song, L. Zhang, J. Zhang, H. Wang and D. P. Wilkinson, *Journal of Power Sources*, 2006, **155**, 95-110.
13. S. Y. Shen, T. S. Zhao, J. B. Xu and Y. S. Li, *Journal of Power Sources*, 2010, **195**, 1001-1006.
14. P. K. Shen and C. Xu, *Electrochemistry Communications*, 2006, **8**, 184-188.
15. I. Merino-Jimenez, M. J. Janik, C. Ponce de Leon and F. C. Walsh, *Journal of Power Sources*, 2014, **269**, 498-508.
16. X. Wang, Y. Tang, Y. Gao and T. Lu, *Journal of Power Sources*, 2008, **175**, 784-788.
17. R. M. Modibedi, T. Masombuka and M. K. Mathe, *International Journal of Hydrogen Energy*, 2011, **36**, 4664-4672.
18. C. Jin, X. Sun, Z. Chen and R. Dong, *Materials Chemistry and Physics*, 2012, **135**, 433-437.

19. M. Nie, H. Tang, Z. Wei, S. P. Jiang and P. K. Shen, *Electrochemistry Communications*, 2007, **9**, 2375-2379.
20. J. B. Xu, T. S. Zhao, S. Y. Shen and Y. S. Li, *International Journal of Hydrogen Energy*, 2010, **35**, 6490-6500.
21. J. Cai, Y. Huang and Y. Guo, *Electrochimica Acta*, 2013, **99**, 22-29.
22. A. O. Neto, M. M. Tusi, N. S. de Oliveira Polanco, S. G. da Silva, M. Coelho dos Santos and E. V. Spinacé, *International Journal of Hydrogen Energy*, 2011, **36**, 10522-10526.
23. Z. Qi, H. Geng, X. Wang, C. Zhao, H. Ji, C. Zhang, J. Xu and Z. Zhang, *Journal of Power Sources*, 2011, **196**, 5823-5828.
24. Z. Liu, X. Zhang and L. Hong, *Electrochemistry Communications*, 2009, **11**, 925-928.
25. M. R. Tarasevich, V. N. Titova, A. A. Yavich, N. V. Petrova and V. A. Bogdanovskaya, *Russ. J. Phys. Chem.*, 2009, **83**, 1850-1854.
26. J. C. Castro, R. M. Antoniassi, R. R. Dias, M. Linardi, E. V. Spinacé and A. O. Neto, *Ionics*, 2012, **18**, 781-786.
27. H. An, H. Cui, D. Zhou, D. Tao, B. Li, J. Zhai and Q. Li, *Electrochimica Acta*, 2013, **92**, 176-182.
28. H. An, L. Pan, H. Cui, B. Li, D. Zhou, J. Zhai and Q. Li, *Electrochimica Acta*, 2013, **102**, 79-87.
29. J. Tayal, B. Rawat and S. Basu, *International Journal of Hydrogen Energy*, 2011, **36**, 14884-14897.
30. V. Bambagioni, C. Bianchini, A. Marchionni, J. Filippi, F. Vizza, J. Teddy, P. Serp and M. Zhiani, *Journal of Power Sources*, 2009, **190**, 241-251.
31. J. M. Jacob, P. G. Corradini, E. Antolini, N. A. Santos and J. Perez, *Applied Catalysis B: Environmental*, 2015, **165**, 176-184.
32. S. Meenakshi, K. G. Nishanth, P. Sridhar and S. Pitchumani, *Electrochimica Acta*, 2014, **135**, 52-59.
33. X. Xue, J. Ge, T. Tian, C. Liu, W. Xing and T. Lu, *Journal of Power Sources*, 2007, **172**, 560-569.
34. M. Uchida, Y. Aoyama, M. Tanabe, N. Yanagihara, N. Eda and A. Ohta, *Journal of the Electrochemical Society*, 1995, **142**, 2572-2576.
35. D.-J. Guo and H.-L. Li, *Journal of Power Sources*, 2006, **160**, 44-49.
36. H. S. Nalwa, *Nanostructured Materials and Nanotechnology (Concise edn.)*, Academic Press, San Diego 2002.
37. S. Tang, G. Sun, J. Qi, S. Sun, J. Guo, Q. Xin and G. M. Haarberg, *Chinese Journal of Catalysis*, 2010, **31**, 12-17.
38. N. Karousis, N. Tagmatarchis and D. Tasis, *Chemical Reviews*, 2010, **110**, 5366-5397.
39. Osorio A. G., Silveira I. C. L., Bueno V. L. and B. C. P., *Applied Surface Science*, 2008, **255**, 2485-2489.
40. A. M. Zaiton, A. M. S. Nur, A. B. Nor and S. Shafinaz, *Journal of Fundamental Sciences*, 2010, **6**, 51-55.
41. Rike Y., Holia O.S., Yukie S., Tadahisa I. and J.-i. A., *The Open Materials Science*, 2011, **5**, 242-247.
42. Z.-M. Dang, L. Wang and L.-P. Zhang, *Journal of Nanomaterials*, 2006, **2006**, 1-5.
43. M. A. Pimenta, G. Dresselhaus, M. S. Dresselhaus, L. G. Cancado, A. Jorio and R. Saito, *Physical Chemistry Chemical Physics*, 2007, **9**, 1276-1291.
44. G. E. Romanos, V. Likodimos, R. R. N. Marques, T. A. Steriotis, S. K. Papageorgiou, J. L. Faria, J. L. Figueiredo, A. M. T. Silva and P. Falaras, *Journal of Physical Chemistry C*, 2011, **115**, 8534-8546.
45. A. E. Daugaard, K. Jankova, J. M. R. Marín, J. Bøgelund and S. Hvilsted, *European Polymer Journal*, 2012, **48**, 743-750.
46. H. Hu, B. Zhao, M. E. Itkis and R. C. Haddon, *The Journal of Physical Chemistry B*, 2003, **107**, 13838-13842.
47. M. W. Marshall, S. Popa-Nita and J. G. Shapter, *Carbon*, 2006, **44**, 1137-1141.
48. Y.-T. Shieh, G.-L. Liu, H.-H. Wu and C.-C. Lee, *Carbon*, 2007, **45**, 1880-1890.
49. A. G. Osorio, I. C. L. Silveira, V. L. Bueno and C. P. Bergmann, *Applied Surface Science*, 2008, **255**, 2485-2489.
50. K. S. W. Sing, D. H. Everett, R. A. W. Haul, L. Moscou, R. A. Pierotti, J. Rouquerol and T. Siemieniewska, in *Handbook of Heterogeneous Catalysis*, Wiley-VCH Verlag GmbH & Co. KGaA, 2008, DOI: 10.1002/9783527610044.hetcat0065.
51. H. Y. Quan, X. H. Peng, B. Shuo, Z. W. Mao and M. C. Hui, *Chem. Phys Lett.*, 2001, **345**, 18-24.
52. S. Inoue, N. Ichikuni, T. Suzuki, T. Uematsu and K. Kaneko, *Phys. Chem.*, 1998, **102**, 4689-4692.

53. N. Jha, P. Ramesh, E. Bekyarova, X. Tian, F. Wang, M. E. Itkis and R. C. Haddon, *Scientific Reports*, 2013, **3**, 2257.
54. S. Jongsomjit, K. Sombatmankhong, S. Mori and P. Prapainainar, PACCON2014 (Pure and Applied Chemistry International Conference 2014) conference proceeding , January 8-10, 2014, Khon Kaen, Thailand.
55. D. He, C. Zeng, C. Xu, N. Cheng, H. Li, S. Mu and M. Pan, *Langmuir*, 2011, **27**, 5582-5588.
56. D. He, Y. Jiang, H. Lv, M. Pan and S. Mu, *Applied Catalysis B: Environmental*, 2013, **132–133**, 379-388.
57. F. N. Qingfeng Yi, Lizhi Sun, *fuel* 2011, **90**, 2617-2623.
58. Z.-L. Liu, R. Huang, Y.-J. Deng, D.-H. Chen, L. Huang, Y.-R. Cai, Q. Wang, S.-P. Chen and S.-G. Sun, *Electrochimica Acta*, 2013, **112**, 919-926.
59. G. Wu and B.-Q. Xu, *Journal of Power Sources*, 2007, **174**, 148-158.
60. C. Xu, L. Cheng, P. Shen and Y. Liu, *Electrochemistry Communications*, 2007, **9**, 997-1001.
61. Y. Hu, P. Wu, Y. Yin, H. Zhang and C. Cai, *Applied Catalysis B: Environmental*, 2012, **111–112**, 208-217.
62. A. Santasalo-Aarnio, M. Borghei, I. V. Anoshkin, A. G. Nasibulin, E. I. Kauppinen, V. Ruiz and T. Kallio, *International Journal of Hydrogen Energy*, 2012, **37**, 3415-3424.
63. Y.-C. Wei, C.-W. Liu, W.-D. Kang, C.-M. Lai, L.-D. Tsai and K.-W. Wang, *Journal of Electroanalytical Chemistry*, 2011, **660**, 64-70.